# Two-Phase Dynamics and Hysteresis in the PEM Fuel Cell Catalyst Layer with the Lattice-Boltzmann Method

Jonathan B. Grunewald,[1az, *] Navneet Goswami,[2, *] Partha P. Mukherjee,[2b, **] and Thomas F. Fuller[1cz, ***]

[1] School of Chemical and Biomolecular Engineering, Georgia Institute of Technology, Atlanta, GA 30332, United States
[2] School of Mechanical Engineering, Purdue University, West Lafayette, IN 47907, United States

[z] Corresponding authors: tom.fuller@chbe.gatech.edu (T. F. Fuller), grunewjb@gatech.edu (J. B. Grunewald)
[*] Electrochemical Society Student Member
[**] Electrochemical Society Member
[***] Electrochemical Society Fellow
[a] ORCID: 0000 – 0003 – 3094 – 2528
[b] ORCID: 0000 – 0001 – 7900 – 7261
[c] ORCID: 0000 – 0001 – 5474 – 2876

**Abstract**

In this work, a Lattice-Boltzmann-Method (LBM) model for simulating hysteresis in a proton exchange membrane fuel cell (PEMFC) electrode is presented. One of the main challenges hindering study of the cathode catalyst layer (CCL) in PEMFCs is the lack of understanding of two-phase transport and how it affects electrochemical performance. Previously, the microstructure details needed to build an accurate mesoscale model to examine such phenomena have eluded researchers; however, with advances in tomography and focused-ion-beam scanning-electron-microscopy (FIB-SEM), reconstruction of the complex porous media has become possible. Using LBM with these representations, the difficult problem of catalyst layer capillary hysteresis can be examined. In two-phase capillary hysteresis, both the equilibrium saturation position as well as its absolute value depends on the wetting history. Based on the models, it is ascertained that at lower capillary numbers, the liquid begins to undergo capillary fingering – only above a capillary pressure of 5 MPa, a regime change into stable displacement is observed. As capillary fingering does not lead to uniform removal of liquid, the prediction is that because high capillary pressures are needed to change to the regime of stable displacement, wicking is not as effective as the primary means of water removal.

**Keywords** Proton Exchange Membrane Fuel Cells, Cathode Catalyst Layer, Two-phase flow, Capillary Hysteresis, Wicking

## Introduction

Proton exchange membrane fuel cells (PEMFCs) are a promising, non-carbon dioxide producing energy conversion alternative that has the potential to dramatically alter the automotive industry[1-3]. Advances in these electrochemical conversion devices have been driven by optimizing the design and understanding of porous flow-through electrodes. However, there are significant challenges in the fundamental understanding of these porous electrodes that have limited the ability to solve longstanding challenges such as grid-level storage and replacement of the internal combustion engine with electrochemical devices. The primary focus of the modeling work addresses the challenges of the cathode catalyst layer (CCL), since not only does this thin layer make experimental characterization extremely difficult, but also because the oxygen reduction reaction (ORR) is considered the most difficult reaction in common electrochemistry[4]. Additionally, the difficulty in studying the operation of the PEMFC is exacerbated with a lack of understanding of the microfluidics of flow through the porous media. The combination of these factors in addition to the intrinsic difficulties with understanding two-phase flow make the CCL a complex and difficult area to study[2, 5-7].

Because of this difficulty, the usual starting point for modeling has been a macrohomogeneous porous electrode model of the catalyst layer, which account for the complex local geometry with approximations such as the Bruggeman correlation for conductivity[8, 9]. These models intrinsically gloss over the microstructure to instead treat the electrode as a web of parameters such as the length, the porosity, the tortuosity, platinum loading, and others. With some optimization, these various descriptors can control the intimate contact among the three-phase boundary for the best electrode. As research has continued, however, the limitations of this idealization are surfacing; as a key example, the model fails to accurately predict the effect of platinum loading on mass-transfer resistance – it forecasts no effect, whereas experiments show a clear impact[10, 11]. However, despite this experimental confirmation, due to the complex structure of the electrode and its ~10-micron profile, it is quite difficult to do in operando studies[12]. To counter this problem, previous work gives insight into the CCL microstructure with varying amounts of carbon corrosion through FIB-SEM (focused-ion beam scanning electron microscopy) to enable the use of mesoscale modeling techniques, an example of the geometry created from these is shown in Figure 1[12-14].

The main objective of the current research is to expand upon the previous FIB-SEM work and fabricate a simulation framework beyond what continuum models do to describe flow behavior and better understand performance failure mechanisms on a local scale[12-16]. Information about the pore distribution and the histogram of the geometry can be found in the publications of Star et al[12, 13]. These geometries have information about degree of corrosion, which hasn't been seen previously in two-phase studies of the electrode. Here, we study the impact of hysteresis: simulating intrusion and drainage of these real FIB-SEM geometries to study how much liquid remains from the water created during ORR. This problem is a major concern in two-phase flow consideration of the electrode, as it has hardly been studied and is of utmost importance for liquid management – even a 10-12% saturation can drastically affect catalysis[2, 6]. The goal of this project on the modeling side is to use the mesoscale methods of Lattice Boltzmann (LBM) for studying the liquid-vapor interface as well as two-phase porous flow and Direct Numerical Simulation (DNS) for solving balance equations and electrochemical effects[17]. This approach is not only useful in the PEMFC community, but also is generally applicable for describing transport phenomena in any porous electrode system[18-20]. The focus of this paper in particular is on LBM, which allows us to examine two-phase flow through the FIB-SEM geometries to obtain these imbibition-drain curves based on the capillary pressure (the difference in pressure between the two phases) and the saturation (the number of liquid voxels divided by the total number of voxels).

Modeling of the CCL should move towards the approach taken in the gas diffusion layer (GDL) by Bazylak,[21-23] Thiele,[15, 16] and others: running on tomography images of the actual geometry. The primary reason for this is that the geometry itself is highly heterogenous; as mentioned, the common macrohomogenous model avoids this complexity. This approach, especially at low catalyst loadings, has begun giving inaccurate results as mentioned above[24]. The main reason why real representations of the geometry haven't been adopted by the fuel-cell community is the difficulty in obtaining these images; however, this barrier is gradually being lifted by the community through the work of More[25], Borup[26], Litster,[27] and others[13, 28, 29]. Starting in the mid to late 2000s, LBM has become more popular with the PEMFC community due to its ability to better resolve pore effects, first debuting for the GDL in around 2005 from works by Mukherjee[30], Wang[31], Niu[32], Park[33-35], and others. The work was then expanded to the CCL by Mukherjee[36-38],

and finally has expanded into what is seen today, with 74 papers on Web of Science published on the cathode side since 2018 alone[39-42].

Existing intrusion porosimetry papers, such as these two[43, 44] pore network models use a computational domain of a network of pores and throats with certain radii rather than the actual geometry. Similarly, works employing pore morphology[45, 46], rely on statistical characterization, such as stochastically reconstructed gas diffusion layer. In contrast, LBM can run on the detailed microstructure itself. Additionally, other methods such as finite volume cannot model the complexity of the microstructure without inordinately long run times. LBM requires the least number of approximations compared to other methods such as pore network, which can only run on idealized microstructures. Pore morphology methods accurately modeling the draining and filling seen in the hysteresis curves, but still require an approximation of a model system for filling the geometry[47]. In comparison to other LBM work, this is one of the first in the cathode to use something other than the Shan-Chen method to look at multi-phase/multi-component flows in addition to examining corroded vs non corroded geometries from the FIB-SEM geometries.

In terms of what literature LBM models show, there is a significantly higher diversity of models in the GDL versus the CCL – this is due to the three order of magnitude difference in pore size between the GDL and CCL. Since this initial treatment, many other researchers have incorporated more advanced LBM phenomena into their models, such as Niu[32] as well as Gao[48] using the multi-relaxation time approach (MRT) as their collision operator for better modeling the complex porous media. More recently, Molaeimanesh et al. have modeled ORR on different agglomerates using a fabricated porous media to show oxygen distribution in the CCL[49-51]. Chen used a coupled FVM-LBM model to show the oxygen distribution in and viability of non-noble metal CCL[52-56]. Jinuntuya et al. as well as Niu used a similar LBM model, but instead of stochastically creating geometries, used tomography methods of the GDL to do their LBM simulations[57, 58]. Many more researchers examined water transport in the GDL and CCL through LBM[39-42, 59-64].

In this paper, we will first discuss the intricacies of our LBM model, the free surface modeling approximation that we used, as well as covering the fundamentals of the multi-relaxation time operator from the open-source code we used. From here, we discuss proving our method by running it through a geometry of packed spheres and comparing it to the Leverett-J function commonly used in PEMFC literature[65-68]. In addition, we analyze

wettability by measuring the contact angle for our model against the prominent two-phase LBM model – the Shan-Chen model. Furthermore, we will take the geometries and calculate the relative permeability *versus* saturation relationship to understand two-phase flow through them further. Finally, we pose simulation on two different FIB-SIM geometry domains, one at the beginning of life and another significantly more corroded, for a variety of different capillary pressures to model hysteresis and comment on the effect it has on water management in the catalyst layer. We also want to stress that LBM is not a simple solution; the fundamental challenges of this simulation must be taken into account before using a generic code for a specific microstructure.

**Mathematical Background**

LBM has evolved into a popular method for simulating multiphase, multicomponent fluid flows for complex geometries that standard computational fluid dynamics (CFD) techniques, such as finite difference, finite element, and finite volume methods, struggle to solve[69, 70]. Other PEMFC papers have expounded upon the basics of LBM, such as the particle populations, the single relaxation time operator, and the solid physical foundation in kinetic theory of gases[38, 49, 54, 57]. What we would like to focus on are the exciting possibilities of other methods of LBM, specifically on simulating two-phase flow inside of the CCL as approximately a free-surface flow and the multi-relaxation time operator[32, 48, 69, 71-73].

As a summary based on the work of Attar et al[72]., the basis of a free surface technique is to identify all cells in the geometry as fluid voxels (liquid water), the solid wall of the Pt/C backbone and ionomer, gas voxels (hydrated air), as well as the boundary between the fluid and gas and track the interface of this boundary[72]. To do this, the mass exchange parameter $\Delta M_i(\boldsymbol{x}, t)$ for an interface cell at some voxel $\mathbf{x}$ and its neighboring voxel $\mathbf{x} + \mathbf{e_i}$ is defined as follows:

$$\Delta M_i(\boldsymbol{x}, t) = \begin{cases} 0 & \boldsymbol{x} + \boldsymbol{e_i} \in Gas \\ f_i^{out}(\boldsymbol{x} + \boldsymbol{e_i}, t) - f_i^{out}(\boldsymbol{x}, t) & \boldsymbol{x} + \boldsymbol{e_i} \in Fluid \\ \frac{1}{2}\left(\varepsilon(\boldsymbol{x}, t) + \varepsilon(\boldsymbol{x} + \boldsymbol{e_i}, t)\right)\left(f_i^{out}(\boldsymbol{x} + \boldsymbol{e_i}, t) - f_i^{out}(\boldsymbol{x}, t)\right) & \boldsymbol{x} + \boldsymbol{e_i} \in Interface \end{cases} \quad [1]$$

Here, $\{\mathbf{e_i}\}7$ represents the nondimensional discrete velocity sets seen in D3Q19, $\varepsilon$ is the volume fraction defined as $\varepsilon = M/\rho$, M is the mass of the liquid for a unit volume, $\rho$ is the

density, and $f_i^{out}$ is the outgoing distribution function. This distribution function is defined as the collision step and is given as follows:

$$f_i^{out}(\boldsymbol{x}, t) = f_i^{in}(\boldsymbol{x}, t) - \frac{1}{\tau}\left(f_i^{in}(\boldsymbol{x}, t) - f_i^{eq}(\rho, \mathbf{v})\right) \quad [2]$$

In this equation, $f_i^{in}(\boldsymbol{x}, t)$ is the streaming step distribution function and $\tau$ is the relaxation time. This relationship assumes that we have no external forces – an accurate assumption due to our extremely small Bond number[38]. All the volume fractions can be represented using a method known as volume of fluid (VoF); here we assign a scalar *C* between 0 and 1 to each void voxel in the geometry so that it satisfies the following relationship for all *m* fluids:

$$\frac{\partial C_m}{\partial t} + \mathbf{v} \cdot \nabla C_m = 0 \quad [3]$$

where $C_m$ has to sum to 1 for every void voxel. Note that this relationship is valid in the case that the kinematic viscosity of the gas phase is functionally infinite compared to the liquid[71-74]. This basis is because free surface techniques assume that the fluid mixing only occurs at the interface and not throughout the liquid. We would like to stress that we do not assume the flow inside the PEMFC catalyst layer is a free surface – it is merely an approximation to resolve the density and viscosity ratio issues many other multiphase multicomponent LBM models have in the PEMFC CCL. Effects such as ionomer saturation, condensation, as well as oxygen diffusion through water will be treated in further publications.

In the previous section, we discussed the relaxation time $\tau$. The relaxation time is used to determine the rate at which the collision operator $\Omega_i$ relaxes the particle populations to some equilibrium $f_i^{eq}$. The collision operator most commonly used in LBM is the Bhatnagar, Gross, and Krook (BGK) model, which assumes a single relaxation time. This choice of a single relaxation time is sufficient for stability in a wide variety of CFD simulations. However, certain conditions, such as in porous geometries where the apparent porosity depends on the exact wall location, can lead to a situation where the profile depends not on physical parameters (i.e. the Reynolds number) but instead on the relaxation time[69, 75]. Solutions that depend on computational parameters are not viscosity-independent solutions, which would violate the kinetic theory of gases on which LBM is

based[76]. To counter this problem, there are many other collision operators $\Omega_i$ in the literature; the most common choice for flow simulations on porous geometries is the MRT collision operator. MRT is chosen because it allows for different relaxation times for each of the Q nodes in the geometry rather than one for the whole simulation. This operator is a matrix representation of the relaxation times and is shown below[30, 36, 69].

$$\Omega_i = -\boldsymbol{M}^{-1}\boldsymbol{S}[\boldsymbol{m}(\boldsymbol{x},t) - \boldsymbol{m}^{eq}(\boldsymbol{x},t)]\Delta t \quad [4]$$

where $\boldsymbol{M}$ is the transformation matrix, $\boldsymbol{S}$ is a diagonal matrix of the relaxation times corresponding to $q$ velocities, $\boldsymbol{m}$ are the individual moments, and $\boldsymbol{m}^{\mathrm{eq}}$ is the equilibrium moments. Since the idea of the MRT operator is to relax the individual moments rather than the populations, there are as many relaxation times are there are moments – as an example, this corresponds to 19 for D3Q19 (the 3 dimensions and 19 velocity sets most commonly seen in 3D multiphase, multicomponent flow). The next step is to collide these moments -- one can define a new moment $\boldsymbol{m}_{\mathrm{k}}^{*}$:

$$\boldsymbol{m}_k^* = \boldsymbol{m}_k - \omega\left(\boldsymbol{m}_k - \boldsymbol{m}_k^{eq}\right)\Delta t \quad [5]$$

Now we need to transform back into population space with the following relationship:

$$f_i^* = \sum_k \boldsymbol{M}_{ik}^{-1}\boldsymbol{m}_k^* \quad [6]$$

Once we transform back into population space, we need to stream to the rest of the nodes in the system – this is done in the following way:

$$f_i(\boldsymbol{x} + \boldsymbol{c}_i\Delta t, t + \Delta t) = f_i^*(\boldsymbol{x},t) \quad [7]$$

Once one discretizes the Boltzmann equation and, after combining these definitions, we arrive at the Lattice Boltzmann Equation:

$$f_i(\boldsymbol{x} + \boldsymbol{c}_i\Delta t, t + \Delta t) = f_i(\boldsymbol{x},t) + \Omega_i(\boldsymbol{x},t) \quad [8]$$

One cycle of the LBM algorithm is shown in Figure 2[69].

The advantage of this approach is that one no longer needs to explicitly discretize the underlying fluid flow equations and can instead derive them implicitly. This is achieved by doing Chapman-Enskog expansion around the Knudsen number to get Navier-Stokes. Since the explicit approaches struggle to resolve the advection term in Navier-Stokes, $(\mathbf{v}\cdot\nabla)\mathbf{v}$, implicit schemes are valuable, especially in areas of reactive and porous flow[77, 78]. While LBM has the ability to resolve some of the challenges in the CCL, such as accounting for the pore morphology and rigorously showing the flow profile, it is quite

expensive computationally. However, this approach is inherently parallel, which makes it run efficiently on clustered supercomputers[79]. This means that one simulation of one million degrees of freedom can reach steady-state in a matter of 12 hours. In the past ten years, these clustered supercomputers have become more accessible to use, meaning these methods have become more common to analyze increasingly complex microstructures.

**Computational Methodology**

The primary goal is to simulate the operation of the PEMFC CCL: this involves modeling the humidified air coming from the GDL and the microporous layer (MPL) and how it interacts with the liquid water formed from ORR. The rigorous simulation of liquid water formation from ORR is beyond the scope of this paper – we are concerned with how this two-phase flow moves on a local level inside of the electrode microstructure. This is a challenging simulation, due to the tortuous path through this microstructure as well as because the density ratio of liquid water to hydrated air is on the order of 1000:1. Standard LBM techniques in the PEMFC literature such as using a single relaxation time as well as the Shan-Chen model (a method of describing the cohesive and adhesive forces seen in two-phase flow with an interparticle force constant G, as well as altering the equation of state with a pseudo potential) become unstable for porous geometries and density ratios above 2:1, respectively[80, 81]. Therefore, we advise using alternate methods from the LBM literature to get around these deficiencies.

The main simulation attempted is flow of oxygen, nitrogen, water vapor, and liquid water through the FIB-SEM data at constant temperature of 353 K. For this, a D3Q19 LBM simulation for free-surface flow using MRT dynamics was conducted. D3Q19 was used because it is the standard for pore scale LBM models[38, 49, 52, 53]. As for why it is the standard, lower 3D velocity sets (such as D3Q13 and D3Q15) have issues – these include either exhibiting checkerboard instability (D3Q13) and thus require additional treatment within MRT to provide accurate solutions or simply are not accurate enough for porous geometries due to the highly heterogenous geometry as mentioned in the sources above (D3Q15)[69, 82]. As for higher velocity sets, the reasoning is similar to the previous response: the increase in accuracy is not sufficient for the drastic increase in computational cost for such a low Reynolds number flow[69, 83, 84]. MRT is used to properly model porous geometry as previously mentioned. To avoid the density ratio instabilities, we have used an interface-based approach to effectively bypass the issue and track the interface with the method

described above rather than explicitly treating the liquid/vapor interactions by solving the Navier-Stokes equations. A VoF approach was used to track the liquid/vapor interface[32, 71, 73, 81, 85-88]. In LBM, boundaries are applied throughout the whole geometry; this means one needs to have a schema for all areas where the Boltzmann equation is solved and where it is not. To do this schema, a bounce-back system was applied; this system means that whenever the simulation reaches a solid boundary, it "bounces back" to the previous node and goes to the next wet-node where the system is solved. For both the gas and liquid phase in the *x*-*y* direction, periodic boundary conditions are used. These were chosen based on the FIB-SEM data: in the *x*/*y* dimensions, only a small portion is captured, whereas, in the *z* direction, the portion accounts for a significant fraction of the CCL (between 30-40%). In this series of simulations, a constant pressure boundary is set at the inlet and no flux boundary at the outlet. Once the simulation begins, it is then iterated over until convergence in the average volume fraction is reached (a difference in each simulation on the order of $O(10^{-4})$). All simulations were carried out in C++ using the Palabos library, a commonly used resource in the geology community[79]. Latt et al. provide more information on how Palabos handles curved surfaces, resolution, and other modeling details.[89]

In this work, the class of simulations attempted describes an infinite film of water on the membrane boundary in the *z* direction; i.e., through the plane of the electrode. From here, liquid flows from the film based on an applied capillary pressure until it reaches a steady-state saturation in the geometry. Here, saturation is measured by the ratio of filled voxels over the available number of void voxels before any water is in the geometry. To get the capillary pressure, one needs to use the time step dt and spacing dx. These quantities were derived by scaling the equations for the Reynolds number observed in the catalyst layer is of $O(10^{-4})$, the desired capillary pressure bound at steady-state, and the lattice kinematic viscosity. These were described in the following equations:

$$\mathrm{Re} = \frac{l^* U^*}{c_s^2 \left(\tau^* - \frac{1}{2}\right)} \qquad [9]$$

$$p_c = \frac{dx^2}{dt^2} * c_s^2 \qquad [10]$$

$$\upsilon = c_s^2 * \left(\tau^* - \frac{1}{2}\right)\frac{dx^2}{dt} \quad [11]$$

In these equations, $l^*$ is the number of lattice sites along the main flow direction, $U^*$ is the velocity scaled over the max velocity of the system, $c_s^2$ is the lattice speed of sound squared (1/3 for the D3Q19 system), $\tau^*$ is the average relaxation time, and $\upsilon$ is the kinematic viscosity of the system in lattice units. One can balance the parameters to get the desired steady-state capillary pressure. This sort of simulation approach is critical for validating the method as well as for analyzing hysteresis – by varying the capillary pressure, one can simulate intrusion porosimetry, allowing for accurate measurements not seen in standard continuum models. As such, the boundary conditions for this simulation were the infinite film of water at the membrane and a held constant capillary pressure at the GDL/MPL boundary. This test is where the invading fluid penetrates the geometry to study the difference in pressure between the two phases.

In these simulations, the goal is to run a specific capillary pressure until the liquid equilibrates inside the geometry to some steady-state saturation. To do this, we started by setting LBM parameters such as the lattice spacing, lattice density, tau, kinematic viscosity, and time step by setting dimensionless numbers like Re and the capillary number (Ca) shown below for a specific class of flow.

$$\mathrm{Ca} = \frac{\mu V}{\sigma} \quad [12]$$

Where, in the equation above, $\mu$ is the visocity, $V$ is the characteristic velocity, and $\sigma$ is the surface tension. From here, a new capillary pressure is set to run from the previous liquid state until the geometry is full (the imbibition). To drain, the process is repeated in reverse until the geometry is empty. Any difference in saturation between the imbibition and drain curves is the hysteresis, which is quantitatively not easily ascertained from traditional models of the PEMFC electrode. As Palabos simulates in the *x* direction, all simulation details and the geometry have been rotated 90 degrees so that the through plane of the electrode is the *x* direction. For the liquid, an infinite film was placed in the *x* direction for the first 15 voxels and all of the *y*/*z* voxels. This process was completed on several different representative volume elements (RVEs) and FIB-SEM geometries to obtain these curves based on work from Goswami[90]. The RVE that best represented the geometry in question while allowing for acceptable run times was the 90x90x(*z*) cubic voxel geometry, where *z* represents the number of slices in the FIB-SEM dataset for that geometry. For these

simulations, $z$ ranges between 90 and 185. For example, $z$ = 90 represents around 0.45x0.59x1.80 micrometers of the CCL in physical units. This corresponds to a lattice spacing around 2 nm. Additionally, the convergence criteria were when the lattice internal energy, defined as the following, changed by less than 0.0001.

$$E = \rho \mathrm{v}^2 \quad [13]$$

In future work, a second class of simulations involves randomly generating liquid throughout the geometry based on platinum loading and the current density, where 100% relative humidity air is flowed from the MPL/GDL boundary. This is more in tune with the operation of the PEMFC. As stated before, LBM cannot model electrochemical effects beyond a basic source term, and as such, these simulations are beyond the scope of the paper.

**Simulation Verification**

To have confidence in the results from LBM or any CFD, one needs to perform test cases to verify it before moving to the goal simulation. For our purposes, we have chosen two common cases in the PEMFC and LBM literature in addition to the relative permeability as a function of saturation relationship. First, we simulate a capillary pressure *versus* saturation relationship and compare this to the Leverett-J function, which is shown below.

$$p_c = \gamma \cos\theta \left(\frac{\varepsilon}{k}\right) J(s) \quad [14]$$

$$J(s) = \begin{matrix} 1.417(1-s) - 2.120(1-s)^2 + 1.263(1-s)^3 & \text{if } \theta < 90 \\ 1.417s - 2.120s^2 + 1.263s^3 & \text{if } \theta > 90 \end{matrix}$$

Here, $p_c$ is the capillary pressure, $\gamma$ is the surface tension, $\theta$ is the contact angle, $\varepsilon$ is the porosity, $k$ is the permeability, and $s$ is the saturation. This relationship is commonly used in the PEMFC community for a general model and was originally developed for flow through packed spheres by Fatt in the 1950s[65-68, 91-93]. This has since been adapted to the CCL with an approach known as the modified Leverett-J function to capture the specifics of the microstructure, but for this analysis, we are looking at the original function to have an equal comparison. Second, we will be looking at the water drop test for wettability. This test describes how well the simulation models contact angles and will show how the free surface model visually aligns with the aforementioned Shan-Chen model for a variety of wetting and nonwetting contact angles.

The goal is to understand the relationship between capillary pressure and saturation inside of the CCL. This is typically done by looking at the capillary pressure *versus* saturation curve, which describes two-phase flow between the wetting (contact angle less than 90° -- the ionomer and fluid components themselves) and the nonwetting phase (contact angle greater than 90° -- the carbon media and Pt). A common constitutive equation for capillary pressure is the Young-Laplace equation below relating it to physical parameters:

$$p_c = \frac{2\gamma \cos\theta}{a} \quad [15]$$

In this equation, $p_c$ is the capillary pressure, $\gamma$ is the surface tension, $\theta$ is the contact angle, and $a$ is the pore size. One typically determines capillary pressure experimentally with mercury intrusion porosimetry (MIP) or another similar test. For the kinds of pore sizes and contact angles in CCLs, capillary phenomena should start occurring around 2 MPa based on an average pore radius of 40 nm, a surface tension of 0.06126 N/m, and a contact angle of 135[12]. However, these kinds of pressures in the CCL are extremely difficult to measure accurately with any experimental method. As such, experimental literature values vary wildly for many of the CCL, with variations by three to four orders of magnitude[65-68, 94-97]. This was why this is ideally used as the test case for LBM, as we can run the simulation through a bed of packed spheres to analytically and visually describe the filling of the spherical geometry. Here, a 90x90x90 voxel geometry of spheres with a void fraction of 0.3004 was filled via the infinite film with varying capillary pressures. The spheres were varying sizes with an average overall pore size of 40 nm. The permeability was calculated using the Carman-Kozeny equation[98] and were on the order of ($10^{-18}$) $m^2$, the surface tension was chosen as water at 353 K (0.06126 N/m), and the porosity and pore radius came from the data set. The curve as well as the visual representation at 3 MPa are shown below in Figure 3.

In the simulation attempted here, the capillary pressures varied between 0.25 MPa to 4 MPa – this bed of packed spheres had similar characteristics to the CCL microstructure. These also were chosen to describe below and above the capillary pressure estimated from the Young-Laplace equation. Additionally, the simulation reached 100% saturation at 4 MPa, meaning that there was no purpose to simulate higher capillary pressures. To compare the two models, a paired t-test was done, which led to t value of 2.2544, meaning

that the difference between the two curves is not statistically significant for a 95% confidence interval. Despite this, there is more deviation from the Leverett-J function at higher capillary pressures. This is acceptable for our analysis, as it is quite difficult to model multiple MPa capillary pressures inside the electrode – for PEMFC capillary pressure models, the modified Leverett-J used by Kumbur and Mench use a piecewise-defined function to describe the eponymous J function for different saturation thresholds[65]. However, since saturation varies quite a bit between the capillary pressures, we decided to do the comparison between the non-modified Leverett-J function for low saturations to avoid discontinuities. Visually, we can move our analysis to what we should be seeing based on liquid profile inside this geometry for a specific set of dimensionless numbers, specifically the capillary number shown below and viscosity ratio. Based on these, at higher capillary pressures, we should see a regime of stable displacement, whereas for lower ones, we should see a regime of capillary fingering. In Figure 3, we see this split between regimes – in the modeled results, there is a large inflection beginning between 1-2 MPa where there is a significant rise in saturation. This is congruent with what we see in the Young-Laplace equation. Below this capillary pressure, there isn't nearly as much increase in saturation for a change in capillary pressure. For the visual results, we see the regime of stable displacement, where the liquid is in a film around the bed of packed spheres. As we can see here, the model results match the Leverett-J model fairly well for the bed of packed spheres, especially for the region of lower capillary pressures.

In order to test the contact angle algorithm and the free surface assumptions for our LBM model, tests were run comparing the results to a more standard two-phase LBM model: the Shan-Chen model more commonly used in the literature[38, 99, 100]. Briefly[69], if one defines the macroscopic velocity $u^{eq}$ as:

$$u^{eq} = \boldsymbol{u}^* + \frac{\tau \boldsymbol{F}}{\rho} \quad [16]$$

Where **u*** and **F** are defined as the following:

$$u^* = \frac{\sum_i f_i \boldsymbol{c}_i}{\rho} \quad [17]$$

$$\boldsymbol{F} = \boldsymbol{F}_c + \boldsymbol{F}_{ads} + \boldsymbol{F}_{ext} \quad [18]$$

$\boldsymbol{F}_c$ and $\boldsymbol{F}_{ads}$ are the cohesive and adhesive forces respectively and $\boldsymbol{F}_{ext}$ is the external body force, which, as mentioned previously, is zero in a PEMFC due to extremely low Bond number. In the Shan-Chen model, the cohesive and adhesive forces are related to the interparticle force constant *G* by the following relationship

$$\boldsymbol{F}_c = -G_c\psi(\boldsymbol{x},t)\sum_i w_i\psi(\boldsymbol{x}+c_i t,t)c_i \qquad [19]$$

$$\boldsymbol{F}_{ads} = -G_{ads}\psi(\boldsymbol{x},t)\sum_i w_i s(\boldsymbol{x}+c_i t,t)c_i \qquad [20]$$

Here, $w_i$ is the weighting at each voxel *i*, and $G_c$ and $G_{ads}$ are the interparticle constant for cohesion and adhesion, respectively. This parameter is often between -2.0 and 2.0. The $s(\boldsymbol{x}+c_i t,t)$ term is either 0 or 1 for void or solid phases, respectively. Finally, the $\psi$ terms all describe the equation of state – this is the most commonly changed parameter in the literature among multiphase models, and for the original Shan-Chen model, it is as follows:

$$\psi(\boldsymbol{x},t) = \psi_0 \exp\left(-\frac{\rho_0}{\rho}\right) \qquad [21]$$

Where $\psi_0$ and $\rho_0$ are arbitrary constants that describe the equation of state. However, the problems start in equation 19, where this equation of state creates numerical instabilities as the density ratio between the two phases rises. As mentioned, this is a prominent model used in the fuel-cell literature, as well as in fields where the density ratio is less than 2:1, such as oil extraction.

Effectively, this test allows us to conclude both that the contact angle algorithm is measured accurately for our 1000:1 density ratio test, as well as conclude that wettability is properly modeled. For our purposes, the density ratio is 2:1 – this allows for a comparison where the Shan-Chen model is valid. The Shan-Chen model is adapted from work done by Santos et al[100]. This test involves modeling a single water drop on a surface of varying contact angles and measuring the curvature of the drop. In Shan-Chen models, typically this is varied with the interparticle force constant G for a linear relationship – here, we will compare the drops in the two models to show how well they model contact angle. The various contact angles shown in Figure 4 are 1, 90, and 135 degrees, chosen for their applicability in PEMFC[101] (1 degrees for ionomer, 135 degrees for the Pt/C phase), as well

as the split between the wetting and nonwetting regimes. For the Shan-Chen model, a wetting and nonwetting contact angle were shown at 20 degrees and 140 degress. The results of this are seen below in Figure 4. In these results, both the Shan-Chen and the free surface model depict the classical signs of the drop deforming for a specific contact angle. The similarity lends credence that the free surface model can get around the density ratio issue we see in the Shan-Chen case.

To have a further understanding of the two-phase flow inside of the microstructure, the relative permeability for each phase was calculated using the methodology outlined by Koido et al.[102] and further applied by Mukherjee[38]. From a reconstructed voxel image, they first used a single-phase LBM approach to calculate the absolute permeability. The single-phase LBM in our paper was an updated version of the program written by Latt and Degruyter[79]. Taking the saturation profile from their two-phase LBM, Koido et al. then calculated the relative permeability using the following relationships:

$$\frac{k_{rg}}{k_{abs}} = \frac{\text{All Gas Voxels}}{\text{Total Voxels}} \quad [22]$$

$$\frac{k_{rl}}{k_{abs}} = \frac{\text{All Liquid Voxels}}{\text{Total Voxels}} \quad [23]$$

$k_{rg}$ and $k_{rl}$ are calculated by taking the saturation profiles at each point on the imbibition curve and changing all liquid voxels to solid for $k_{rg}$ and all gas voxels to solid for $k_{rl}$. From here, each new geometry created is iterated through with the single-phase LBM to calculate a permeability. The relative permeability for each phase is the ratio between this permeability and the absolute permeability. The resultant relative permeabilities were then compared to compared to a commonly used fitted model for the GDL from Koido et al. shown below[102]:

$$k_{rg} = (1 - s)^5 \quad [24]$$

$$k_{rl} = Max(1.089(s^{1.5} - 1) + 1{,}0) \quad [25]$$

Here, *s* refers to the saturation. The results from the LBM relative permeability calculation and the comparison to the model for the film study is shown below.

The absolute permeability computed in lattice units was 0.6544. Comparing to the model as well as results from Mukherjee, the two-phase correlations calculated here show expected trends: at low levels of saturation, most of the permeability can be explained by the gas phase, whereas as the geometry fills, the liquid phase controls most of the

permeability. This is important to show not only to give a parameter for direct comparison to other LBM two-phase models of the microstructure, but also to give insight to larger PEMFC CCL models that take into account the electrochemistry.

**Results and Discussion**

After building and testing the model above, our primary goal is to use it to explore phenomena that are difficult to simulate in standard continuum models or measure experimentally. As mentioned in previous work, many LBM models of the PEMFC electrode either do not attempt to explore the issues above or use insufficient methods to model the difficult multicomponent, multiphase simulations through porous geometries. Examples of these insufficient methods include using stochastic geometries or methods that cannot account for the density ratio. As such, we will be looking at hysteresis, which not only is difficult to see in continuum models as well as experimentally[43, 68, 96, 97, 103], but also is critical to examining flooding in PEMFC electrodes[5, 6].

As noted previously, the way we model hysteresis is to simulate MIP with different capillary pressures in the *x* direction. This process is done by setting a constant pressure boundary at the inlet and no flux boundary at the outlet, as well as periodic bounds in the *y*/*z* direction – this is shown in Figure 6. At steady-state, we would expect to see a constant capillary pressure for a specific saturation through each slice of the FIB-SEM geometry. Once the simulation reaches steady-state, the previous saturation profile is then used for the next capillary pressure intrusion and allowed to reach steady-state, continuing until 10 MPa. The range of 0.25 MPa to 10 MPa was chosen because this was the point where the geometry completely filled up (i.e., reaching 100% saturation) as well as reached a range of values above and below the prediction for the Young-Laplace equation. To model the drainage portion of the curve, this process is then repeated in reverse: liquid leaves from the geometry back into the film and allowed to reach steady-state. Any difference between the two curves is attributed to capillary hysteresis.

These tests were run on three different geometries of varying corrosion: a BOL, a larger amount of corroded electrode, and finally an EOL electrode. The physical dimensions of these electrodes are included in Table 1. The average, equilibrium hysteresis curves are shown below in Figure 7 for the BOL electrode and Figure 8 for the EOL electrode. The middle amount of corrosion electrode is included in supporting information.

The visual sequence of the 3 MPa capillary pressure is shown in Figure 9 for the BOL electrode and Figure 10 for the EOL electrode. The visual for 3 MPa for the middle amount of corrosion is also in supporting information.

As a general conclusion, we see that the two curves begin to deviate at lower capillary pressures. This ideal is what we should expect – as the overall shape of the curve is characterized by a rapid rise in saturation followed by an asymptote at 100% saturation, the majority of the difference should occur in the sharp rise rather than in the tail of the curve. The general shape of the curve can be confirmed from experimental analysis of PEMFC porous media[97]. Also, the overall values obtained – reaching around 100% saturation at between 5-6 MPa – is similar to some of the results seen in the literature for PEMFC catalyst layers. As for the difference between the BOL and EOL microstructures, the overall values are relatively similar – there are some small differences in where the hysteresis curves reach the asymptote as well as the standard errors. This phenomenon is further examined in the visual representation of a point in the sharp increase region that we see in Figures 9-10. In the 3 MPa visual representation, what we see is that as the simulation reaches steady-state, more liquid is concentrated towards the film (i.e., the membrane) even in the beginning stages of the simulation. This is what we would expect: more liquid should be concentrated closer to the center of the electrode than would be towards the GDL/MPL boundary. However, here is where we see major differences in the profile between the two corroded microstructures. The BOL microstructure has a liquid profile that is much more conducive to flow – there aren't many unconnected pores as the liquid conglomerates. However, for the more corroded microstructure, the liquid profile is much more disjointed – there are many unconnected pores which inhibit flow. More information can be gleaned from the dimensionless numbers throughout the simulation. For two-phase flow in porous media, the most important ones are Capillary number (Ca) shown above and the viscosity ratio (M). The latter two describe the phase diagram for capillary phenomena – this is shown in Figure 11 below in work adapted from Mukherjee[38, 104].

In this series of simulations, we begin in the regime of capillary fingering and end in region of stable displacement. We see these locations from our dimensionless number output – at low capillary pressures, our capillary number is $O(10^{-6})$, giving rise to capillary fingering. Capillary fingering can be seen in below where the liquid randomly moves

through the pores and "fingers" without moving as a film. As the capillary pressure increases, the capillary number also increases, reaching a peak of $O(10^2)$. This order of magnitude corresponds to the regime of stable displacement, where the liquid moves in a film through the geometry. The large circles in the phase diagram demarcate the beginning and ending capillary numbers. Note that the viscosity ratio of the fluid, 56.6:1 at 353 K, remains a constant throughout the simulation. What this tells us is that at lower capillary pressures, if the formed liquid water is more concentrated closer to the membrane, we should expect to see more fibrous liquid water distributions in the catalyst layer. This, by extension, may lead to areas with more local flooding here rather than other areas of the CCL. When compared between the two BOL and EOL microstructures, the overall capillary numbers at each point have a non-statistically significant difference. This shows that despite the difference in flow profile, the regimes are still reached at relatively similar capillary numbers.

As mentioned above, the curves for the different RVEs show that at lower capillary pressures, there is a significant (between 5-10 % saturation) hysteresis inside of the geometry. This is critical, as even low levels of saturation can impact PEMFC performance. However, these curves also identify other issues. As mentioned previously, the expected steady-state condition from simulating MIP is that at each capillary pressure, there is a constant saturation. This phenomenon is not what we see; at lower capillary pressures, the saturation profile per slice is not constant, with more of the liquid closer to the membrane than through the geometry until higher capillary pressures. We can explain this through the capillary number mentioned previously, where the regime change occurs around 5 MPa. We see this fact from the drainage portion of the curve; at 1 and 5 MPa on the drainage side, visually shown in Figures 12 and 13, liquid begins to finger back into the films instead of receding as one large film. However, this is where our difficulty resides – this leads to highly incongruent distributions where there is more liquid closer to the membrane than at further from the center of the electrode. At lower capillary pressures, we would expect the liquid to finger from this region out towards the GDL/MPL boundary where it can be removed from phenomena such as wicking. Wicking describes that, due to the hydrophobic media, water will leave the geometry at higher saturations. However, these fingers are ineffective for bulk movement of liquid water – these fingers only account for small amounts of saturation whereas films can allow for liquid to be removed effectively. This

means we predict that wicking is relatively ineffective at removing saturation because of the higher capillary pressure needed to reach this regime. These higher capillary pressures are uncommon in normal operation of the PEMFC.

## Conclusion

This work shows that LBM model can be a chief method for CCL analysis not just in regard to water management, but also elucidating PEMFC phenomena more widely. Studying hysteresis with LBM gives better insight for understanding local saturation and what factors impact liquid transport in the catalyst layer. A better understanding of the CCL response to various operating parameters is essential for advanced PEMFCs, especially with the need to understand two-phase interactions. The model is distinguished from the rest of the literature for two reasons: the first being the use of a CCL geometry reconstructed from FIB-SEM and mesoscale modeling techniques than stochastic reconstruction. The second is, on the LBM side, it examines the issue of density ratios with the use of free surface methods. This two-fold change allows the field to move beyond simply ignoring the microstructure as seen in the macrohomogenous model as well as use the wealth of literature for LBM in the geology fields to analyze the challenging three-phase boundary in the porous CCL. As seen here, we can use these methods to give some insight into difficult problems for the PEMFC field at large. Additionally, we show here that the goal of LBM in PEMFCs is not just to show water movement, but also to tackle important issues in operation. In the past, there has been resistance to using these methods due to their computationally intensive nature and the lack of availability of microstructures; however, we have shown that these are gradually being lifted. Also, given the complexity of the models and the paucity of open-source codes, more collaboration in the PEMFC community and renewed impetus towards openly shared and developed code can foster innovative insights into CCL physics. These efforts will help us design and model PEMFC that can successfully innovate the next generation of energy storage devices.

## Acknowledgement

Financial support from the National Science Foundation (NSF grants: 1805215 and 1805183) is gratefully acknowledged.

## Table of Nomenclature

| Abbreviation | Meaning |
|---|---|

| | |
|---|---|
| LBM | Lattice Boltzmann Method |
| PEMFC | Proton Exchange Membrane Fuel Cell |
| CCL | Cathode Catalyst Layer |
| FIB-SEM | Focused-Ion Beam Scanning Electron Microscopy |
| ORR | Oxygen reduction reaction |
| DNS | Direct Numerical Simulation |
| GDL | Gas Diffusion Layer |
| MRT | Multi-Relaxation Time |
| FVM | Finite Volume Method |
| CFD | Computational Fluid Dynamics |
| VoF | Volume of Fluid Method |
| BGK | Bhatnagar, Gross, and Krook |
| MPL | Microporous Layer |
| D3Q19 | 3 dimensions, 19 velocities |
| RVE | Representative Volume Element |
| MIP | Mercury Intrusion Porosimetry |
| BOL | Beginning of Life |
| EOL | End of Life |

## References


1. M. M. Mench, *Fuel Cell Engines*, John Wiley & Sons, Hoboken, NJ (2008).
2. B. P. Setzler, Vol. Ph. D. Georgia Institute of Technology, Atlanta, 2015.
3. T. F. Fuller, J.N. Harb, *Electrochemical Engineering*, John WIley & Sons, Inc., Hoboken, N.J. (2018).
4. J. Newman, Thomas-Alyea, K.E., *Electrochemical Systems*, John Wiley & Sons, Hoboken, N.J. (2004).
5. A. Z. Weber, R. M. Darling, and J. Newman, *J Electrochem Soc,* **151** (10), A1715-A1727 (2004).
6. A. Z. Weber, R. L. Borup, R. M. Darling, P. K. Das, T. J. Dursch, W. B. Gu, D. Harvey, A. Kusoglu, S. Litster, M. M. Mench, R. Mukundan, J. P. Owejan, J. G. Pharoah, M. Secanell, and I. V. Zenyuk, *J Electrochem Soc,* **161** (12), F1254-F1299 (2014).
7. P. K. Das, A. Grippin, A. Kwong, and A. Z. Weber, *J Electrochem Soc,* **159** (5), B489-B496 (2012).
8. J. Newman and W. Tiedemann, *Aiche J,* **21** (1), 25-41 (1975).
9. J. Giner and C. Hunter, *J Electrochem Soc,* **116** (8), 1124-& (1969).
10. W. Yoon and A. Z. Weber, *J Electrochem Soc,* **158** (8), B1007-B1018 (2011).
11. A. Z. Weber and A. Kusoglu, *J Mater Chem A,* **2** (41), 17207-17211 (2014).
12. A. G. Star, Vol. Ph. D. Georgia Institute of Technology, Atlanta, 2018.
13. A. G. Star and T. F. Fuller, *J Electrochem Soc,* **164** (9), F901-F907 (2017).
14. A. G. Star and T. F. Fuller, *Chem Eng Sci,* **201** 309-318 (2019).
15. M. Klingele, R. Zengerle, and S. Thiele, *J Power Sources,* **275** 852-859 (2015).
16. S. Thiele, R. Zengerle, and C. Ziegler, *Nano Research,* **4** (9), 849-860 (2011).

17. J. B. Grunewald, A. N. Mistry, A. Verma, N. Goswami, P.P. Mukherjee, T.F. Fuller, *J Electrochem Soc,* **166** (7), F3089-F3092 (2019).
18. A. N. Mistry, K. Smith, and P. P. Mukherjee, *Acs Appl Mater Inter,* **10** (34), 28644-28655 (2018).
19. A. N. Mistry and P. P. Mukherjee, *J Phys Chem C,* **122** (32), 18329-18335 (2018).
20. A. N. Mistry, K. Smith, and P. P. Mukherjee, *Acs Appl Mater Inter,* **10** (7), 6317-6326 (2018).
21. A. Bazylak, *Int J Hydrogen Energ,* **34** (9), 3845-3857 (2009).
22. J. Hinebaugh, Z. Fishman, and A. Bazylak, *J Electrochem Soc,* **157** (11), B1651-B1657 (2010).
23. Z. Fishman, J. Hinebaugh, and A. Bazylak, *J Electrochem Soc,* **157** (11), B1643-B1650 (2010).
24. F. C. Cetinbas, S. G. Advani, and A. K. Prasad, *J Power Sources,* **250** 110-119 (2014).
25. K. L. More, *in* "DOE Hydrogen Program". Oak Ridge National Lab, Oak Ridge, TN, 2005.
26. D. S. Hussey, J. M. LaManna, E. Baltic, D. L. Jacobson, S. Stariha, D. Spernjak, R. Mukundan, and R. L. Borup, *Ecs Transactions,* **80** (8), 385-393 (2017).
27. S. Litster, W. K. Epting, E. A. Wargo, S. R. Kalidindi, and E. C. Kumbur, *Fuel Cells,* **13** (5), 935-945 (2013).
28. T. Prill and K. Schladitz, *Scanning,* **35** (3), 189-195 (2013).
29. T. Prill, K. Schladitz, D. Jeulin, M. Faessel, and C. Wieser, *J Microsc-Oxford,* **250** (2), 77-87 (2013).
30. P. P. Mukherjee and C. Y. Wang, *J Electrochem Soc,* **153** (5), A840-A849 (2006).
31. L. P. Wang and B. Afsharpoya, *Math Comput Simulat,* **72** (2-6), 242-248 (2006).
32. X. D. Niu, T. Munekata, S. A. Hyodo, and K. Suga, *J Power Sources,* **172** (2), 542-552 (2007).
33. J. Park, M. Matsubara, and X. Li, *J Power Sources,* **173** (1), 404-414 (2007).
34. J. Park and X. Li, *J Power Sources,* **178** (1), 248-257 (2008).
35. J. Park and X. Li, *Ecs Transactions,* **12** (1), 81-92 (2008).
36. P. P. Mukherjee and C. Y. Wang, *J Electrochem Soc,* **154** (11), B1121-B1131 (2007).
37. P. P. Mukherjee, C. Y. Wang, and Q. J. Kang, *Electrochimica Acta,* **54** (27), 6861-6875 (2009).
38. P. P. Mukherjee, Q. J. Kang, and C. Y. Wang, *Energy & Environmental Science,* **4** (2), 346-369 (2011).
39. P. Satjaritanun, S. Hirano, I. V. Zenyuk, J. W. Weidner, N. Tippayawong, and S. Shimpalee, *J Electrochem Soc,* **167** (1), (2019).
40. S. Shimpalee, P. Satjaritanun, S. Hirano, N. Tippayawong, and J. W. Weidner, *J Electrochem Soc,* **166** (8), F534-F543 (2019).
41. P. S. M. Sepe, S. Hirano, I. V. Zenyuk, N. Tippayawong and S. Shimpalee, *J Electrochem Soc,* **167** (2020).
42. P. Satjaritanun, S. Hirano, A. D. Shum, I. V. Zenyuk, A. Z. Weber, J. W. Weidner, and S. Shimpalee, *J Electrochem Soc,* **165** (13), F1115-F1126 (2018).
43. J. Gostick, *in* "University of Waterloo", Vol. Doctor of Philosophy. University of Waterloo, Waterloo, Ontario, Canada, 2008.

44. M. Sabharwal, J. T. Gostick, and M. Secanell, *J Electrochem Soc,* **165** (7), F553-F563 (2018).
45. R. D. Hazlett, *Transport Porous Med,* **20** (1-2), 21-35 (1995).
46. V. P. Schulz, J. Becker, A. Wiegmann, P. P. Mukherjee, and C. Y. Wang, *J Electrochem Soc,* **154** (4), B419-B426 (2007).
47. M. Hilpert and C. T. Miller, *Adv Water Resour,* **24** (3-4), 243-255 (2001).
48. Y. Gao, *Int J Heat Mass Tran,* **88** 122-132 (2015).
49. G. R. Molaeimanesh and M. H. Akbari, *J Power Sources,* **258** 89-97 (2014).
50. G. R. Molaeimanesh and M. H. Akbari, *Int J Hydrogen Energ,* **40** (15), 5169-5185 (2015).
51. G. R. Molaeimanesh, M. A. Bamdezh, and M. Nazemian, *Int J Hydrogen Energ,* **43** (45), 20959-20975 (2018).
52. L. Chen, H. B. Luan, Y. L. Feng, C. X. Song, Y. L. He, and W. Q. Tao, *Int J Heat Mass Tran,* **55** (13-14), 3834-3848 (2012).
53. L. Chen, Y. L. Feng, C. X. Song, L. Chen, Y. L. He, and W. Q. Tao, *Int J Heat Mass Tran,* **63** 268-283 (2013).
54. L. Chen, G. Wu, E. F. Holby, P. Zelenay, W. Q. Tao, and Q. J. Kang, *Electrochim Acta,* **158** 175-186 (2015).
55. L. Chen, R. Y. Zhang, T. Min, Q. J. Kang, and W. Q. Tao, *Chemical Engineering Journal,* **349** 428-437 (2018).
56. L. Chen, Q. J. Kang, and W. Q. Tao, *Electrochim Acta,* **306** 454-465 (2019).
57. F. Jinuntuya, M. Whiteley, R. Chen, and A. Fly, *J Power Sources,* **378** 53-65 (2018).
58. P. Rama, Y. Liu, R. Chen, H. Ostadi, K. Jiang, X. X. Zhang, R. Fisher, and M. Jeschke, *J Fuel Cell Sci Tech,* **7** (3), (2010).
59. D. Froning, J. Brinkmann, U. Reimer, V. Schmidt, W. Lehnert, and D. Stolten, *Electrochim Acta,* **110** 325-334 (2013).
60. L. Hao and P. Cheng, *Int J Heat Mass Tran,* **53** (9-10), 1908-1913 (2010).
61. L. Hao and P. Cheng, *J Power Sources,* **195** (12), 3870-3881 (2010).
62. J. Hao and L. D. Zhu, *Comput Math Appl,* **59** (1), 185-193 (2010).
63. P. Satjaritanun, E. Bringley, J. R. Regalbuto, J. A. Regalbuto, J. Register, J. W. Weidner, Y. Khunatorn, and S. Shimpalee, *Chem Eng Res Des,* **130** 63-77 (2018).
64. T. Min, L. Chen, Y. M. Gao, and W. Q. Tao, *Enrgy Proced,* **158** 1479-1484 (2019).
65. E. C. Kumbur, K. V. Sharp, and M. M. Mench, *J Electrochem Soc,* **154** (12), B1315-B1324 (2007).
66. E. C. Kumbur, K. V. Sharp, and M. M. Mench, *J Electrochem Soc,* **154** (12), B1305-B1314 (2007).
67. E. C. Kumbur, K. V. Sharp, and M. M. Mench, *J Electrochem Soc,* **154** (12), B1295-B1304 (2007).
68. J. M. LaManna, J. V. Bothe, F. Y. Zhang, and M. M. Mench, *J Power Sources,* **271** 180-186 (2014).
69. T. Kruger, *The Lattice Boltzmann Method*, Springer, Switzerland (2017).
70. M. C. Sukop and D. T. Thorne, *Lattice Boltzmann Modeling: An Introduction for Georscientists and Engineers, 2nd ed.*, Springer (2006).
71. C. Korner, M. Thies, T. Hofmann, N. Thurey, and U. Rude, *J Stat Phys,* **121** (1-2), 179-196 (2005).
72. E. Attar and C. Korner, *J Colloid Interf Sci,* **335** (1), 84-93 (2009).

73. I. Ginzburg and K. Steiner, *J Comput Phys,* **185** (1), 61-99 (2003).
74. E. Attar and C. Korner, *Int J Heat Fluid Fl,* **32** (1), 156-163 (2011).
75. S. Khirevich, I. Ginzburg, and U. Tallarek, *J Comput Phys,* **281** 708-742 (2015).
76. D. d'Humieres and I. Ginzburg, *Comput Math Appl,* **58** (5), 823-840 (2009).
77. R. H. T. Pletcher, J.C.; Anderson, D.A., *Computational Fluid Mechanics and Heat Transfer*, Taylor and Francis Publishers (2013).
78. H. D. Chen, S. Y. Chen, and W. H. Matthaeus, *Phys Rev A,* **45** (8), R5339-R5342 (1992).
79. J. Latt, Vol. 2019.
80. S. Y. Chen, Z. Wang, X. W. Shan, and G. D. Doolen, *J Stat Phys,* **68** (3-4), 379-400 (1992).
81. X. W. Shan and H. D. Chen, *Phys Rev E,* **47** (3), 1815-1819 (1993).
82. M. Junk, A. Klar, and L. S. Luo, *J Comput Phys,* **210** (2), 676-704 (2005).
83. K. Suga, Y. Kuwata, K. Takashima, and R. Chikasue, *Comput Math Appl,* **69** (6), 518-529 (2015).
84. A. T. White and C. K. Chong, *J Comput Phys,* **230** (16), 6367-6378 (2011).
85. W. Sun, B. A. Peppley, and K. Karan, *Electrochim Acta,* **50** (16-17), 3359-3374 (2005).
86. Y. Y. Shao, G. P. Yin, and Y. Z. Gao, *J Power Sources,* **171** (2), 558-566 (2007).
87. I. Ginzburg, F. Verhaeghe, and D. d'Humieres, *Commun Comput Phys,* **3** (2), 427-478 (2008).
88. H. W. Zheng, C. Shu, and Y. T. Chew, *J Comput Phys,* **218** (1), 353-371 (2006).
89. J. Latt, O. Malaspinas, D. Kontaxakis, A. Parmigiani, D. Lagrava, F. Brogi, M. B. Belgacem, Y. Thorimbert, S. Leclaire, S. Li, F. Marson, J. Lemus, C. Kotsalos, R. Conradin, C. Coreixas, R. Petkantchin, F. Raynaud, J. Beny, and B. Chopard, *Comput Math Appl,* **81** 334-350 (2021).
90. N. M. Goswami, A.; Grunewald, J.; Fuller, T.F.; Mukherjee, P.P, *J Electrochem Soc,* **167** (2020).
91. I. Fatt, *Transactions of the American Insitute and Mining and Metallurical Engineers,* **207** 144-159 (1956).
92. I. Fatt, *Transactions of the American Insitute and Mining and Metallurical Engineers,* **207** 160-163 (1956).
93. I. Fatt, *Transactions of the American Insitute and Mining and Metallurical Engineers,* **207** 164-181 (1956).
94. H. P. Gunterman, A. H. Kwong, J. T. Gostick, A. Kusoglu, and A. Z. Weber, *Ecs Transactions,* **41** (1), 647-650 (2011).
95. A. Kusoglu, A. Kwong, K. T. Clark, H. P. Gunterman, and A. Z. Weber, *J Electrochem Soc,* **159** (9), F530-F535 (2012).
96. M. Uchida, Y. Aoyama, N. Eda, and A. Ohta, *J Electrochem Soc,* **142** (12), 4143-4149 (1995).
97. S. Malik, L. Smith, J. Sharman, E. M. Holt, and S. P. Rigby, *Ind Eng Chem Res,* **55** (41), 10850-10859 (2016).
98. P. C. Carman, *Flow of gases through porous media*, Buttsworths, London (1956).
99. P. J. Yin and G. F. Zhao, *Int J Numer Anal Met,* **39** (11), 1188-1211 (2015).
100. J. B. Santos, A.; Landry, C. , Github, 2019.

101. Z. Y. Fang, A. G. Star, and T. F. Fuller, *J Electrochem Soc,* **166** (12), F709-F715 (2019).
102. T. Koido, T. Furusawa, and K. Moriyama, *J Power Sources,* **175** (1), 127-136 (2008).
103. J. T. Gostick, M. W. Fowler, M. A. Ioannidis, M. D. Pritzker, Y. M. Volfkovich, and A. Sakars, *J Power Sources,* **156** (2), 375-387 (2006).
104. R. Lenormand, E. Touboul, and C. Zarcone, *J Fluid Mech,* **189** 165-187 (1988).

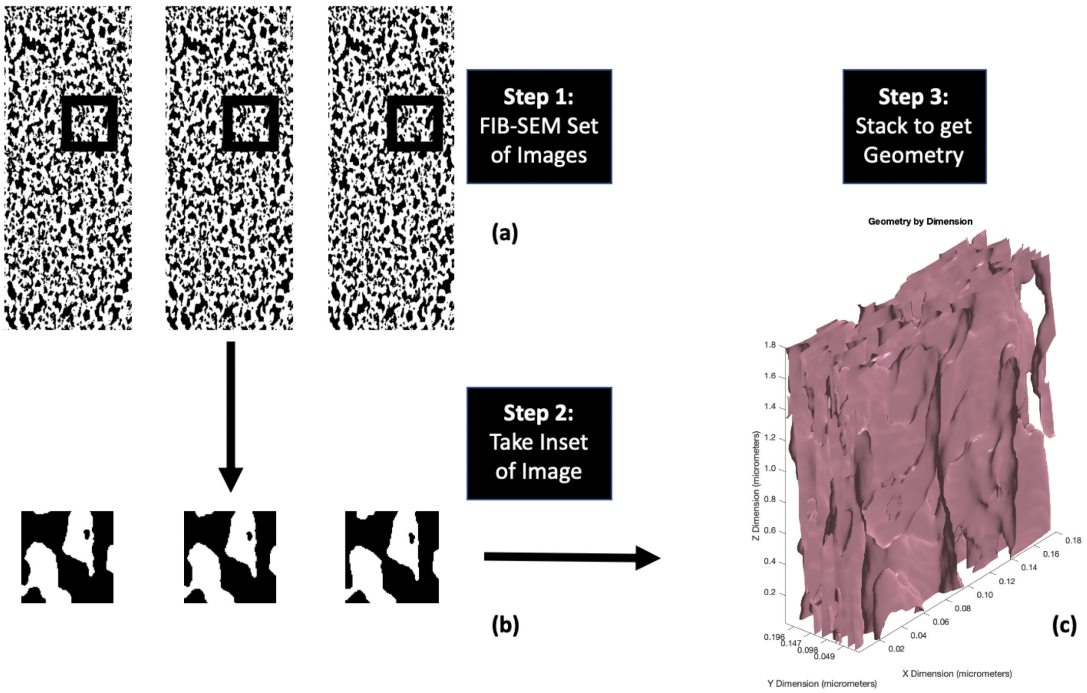


**Figure 1:** An example of geometry creation for LBM. (a) Slices of the segmented FIB-SEM CCL[12]. (b) An example of the portions of geometries from individual slices of the FIB-SEM geometry. (c) Full spacing filling model of geometry created from the portions of the segmented slices.

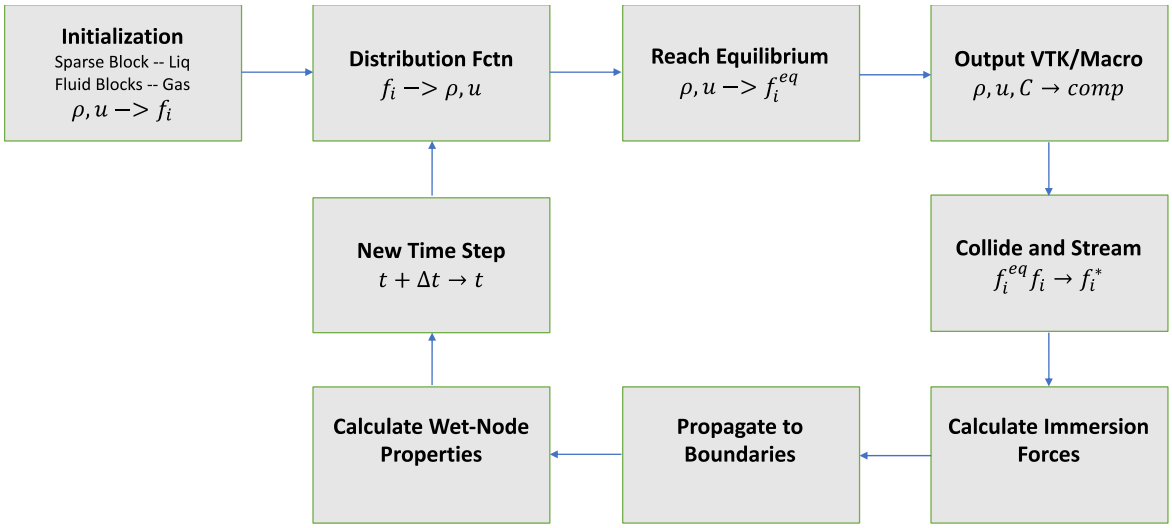


**Figure 2:** One iteration of the LBM algorithm[69]

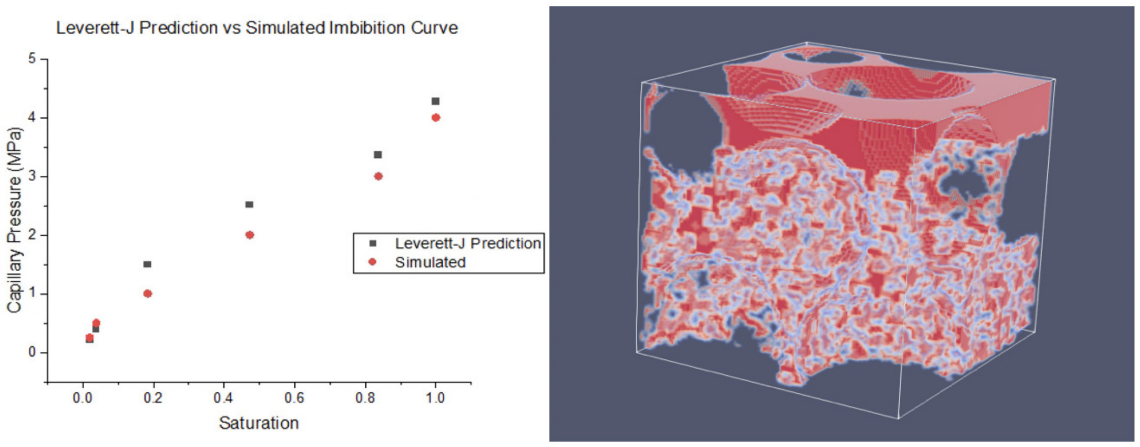


**Figure 3:** (a) Leverett-J model predictions for packed spheres for a non-wetting contact angle of 135 ° and the LBM result. (b) Visual output of the LBM results of the 3 MPa test – here, the red describes the liquid in the geometry, whereas the white hue is the interface between the liquid and vapor.

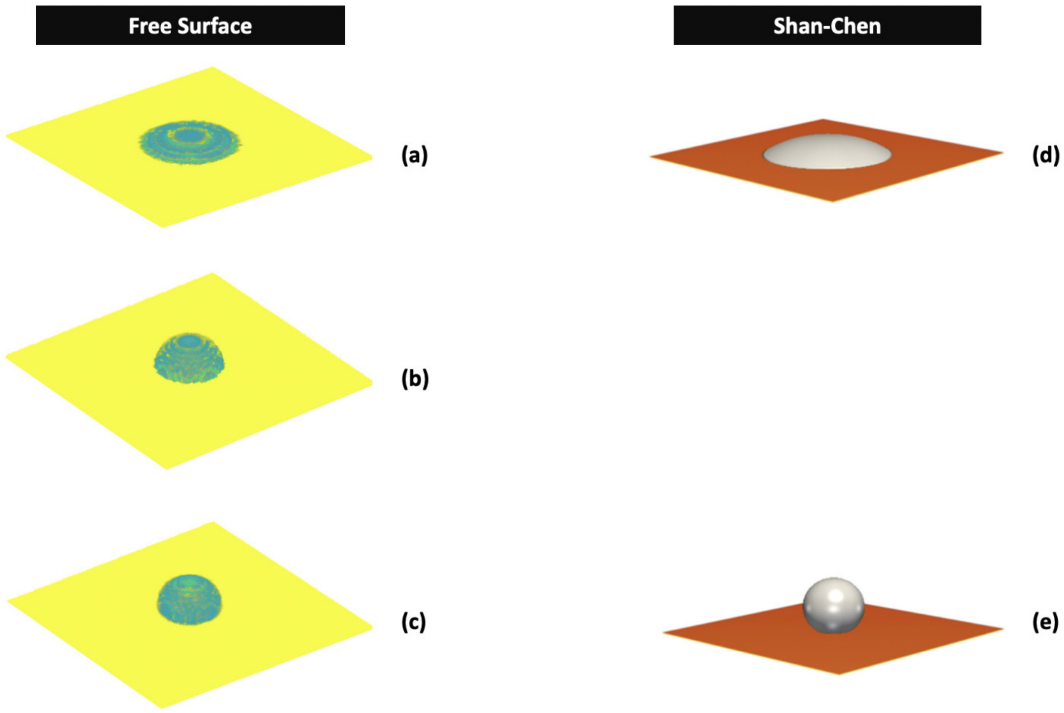


**Figure 4:** Contact angle test of various different contact angles on a flat surface for the free surface (a)-(c) and Shan-Chen (d)-(e) models. The angles measured are (a) 1 degrees, (b) 90 degrees, and (c) 135 degrees for the free surface side, while the Shan-Chen model has a contact angle of (d) 20 degrees and (e) 140 degrees[100].

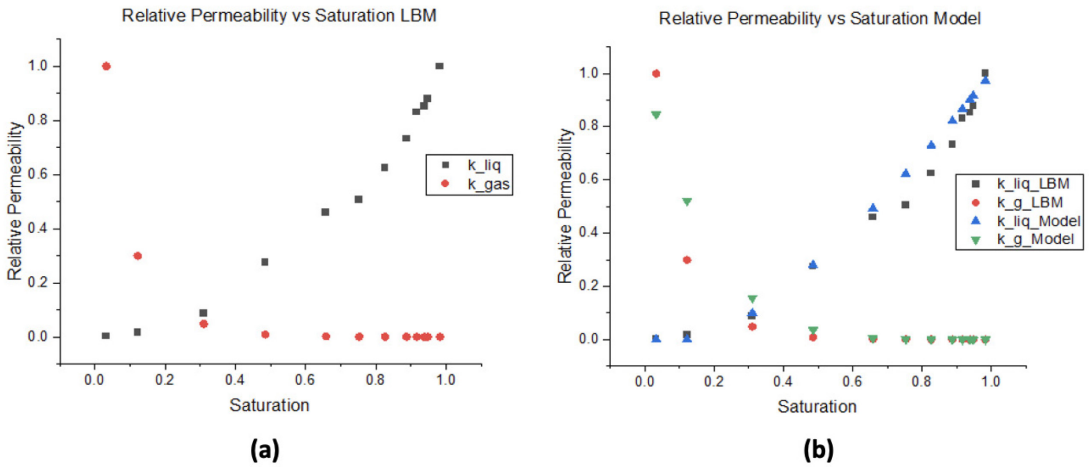


**Figure 5:** Relative permeability *versus* saturation comparisons for LBM (a) and against a literature model (b).

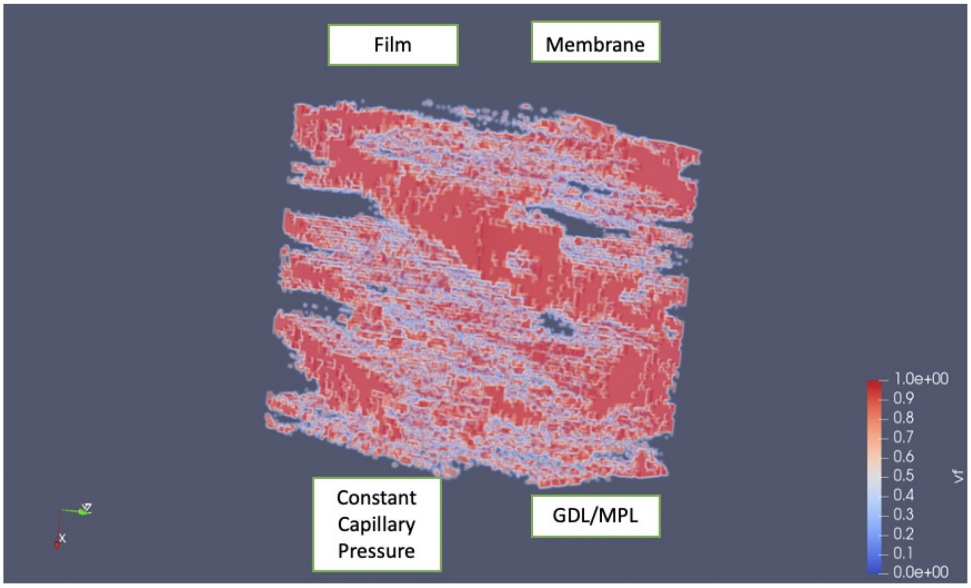


**Figure 6:** Visual Description of boundary conditions with a full geometry

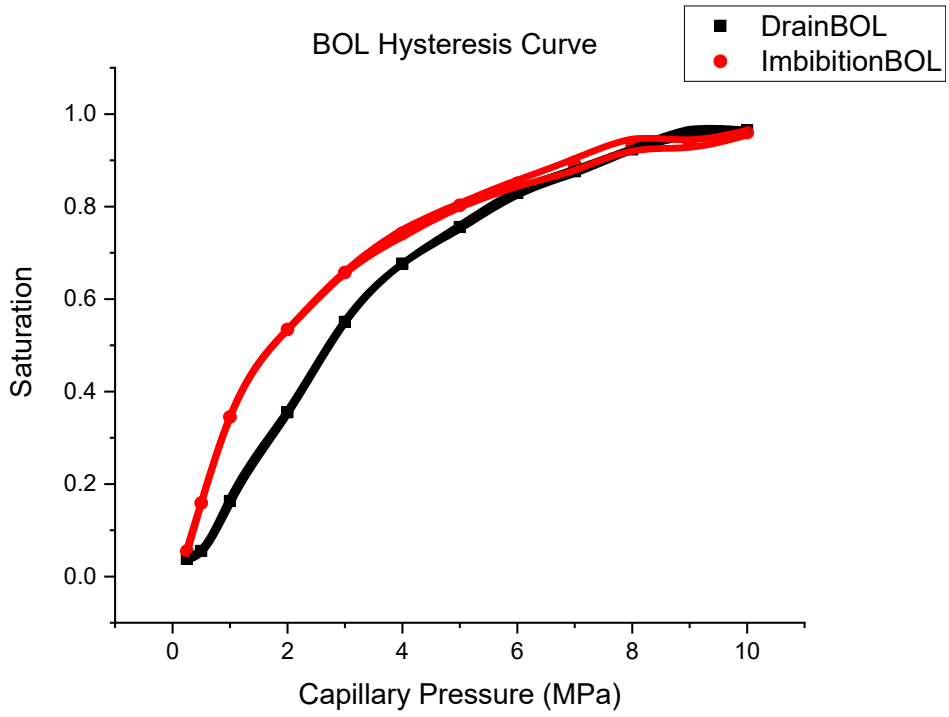


**Figure 7:** 90x90x181 RVE hysteresis curve for various capillary pressures from 0.25 MPa to 10 MPa for the BOL electrode. Curve shows both drainage portion and imbibition for the FIB-SEM geometries.

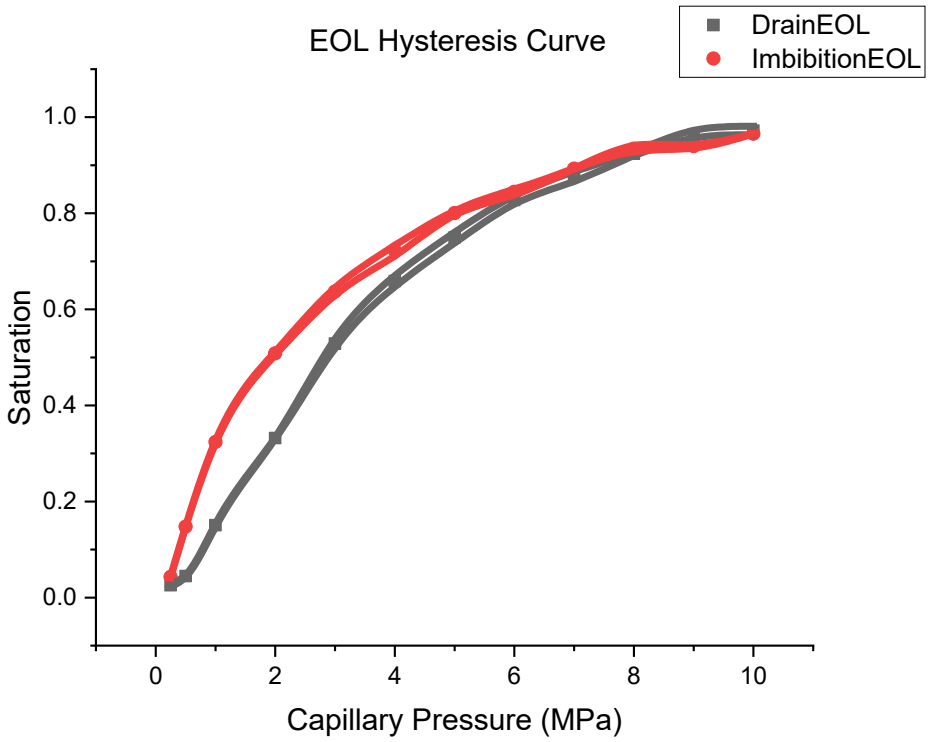


**Figure 8:** 90x90x154 RVE hysteresis curve for various capillary pressures from 0.25 MPa to 10 MPa for the EOL electrode. Curve shows both drainage portion and imbibition for the FIB-SEM geometries.

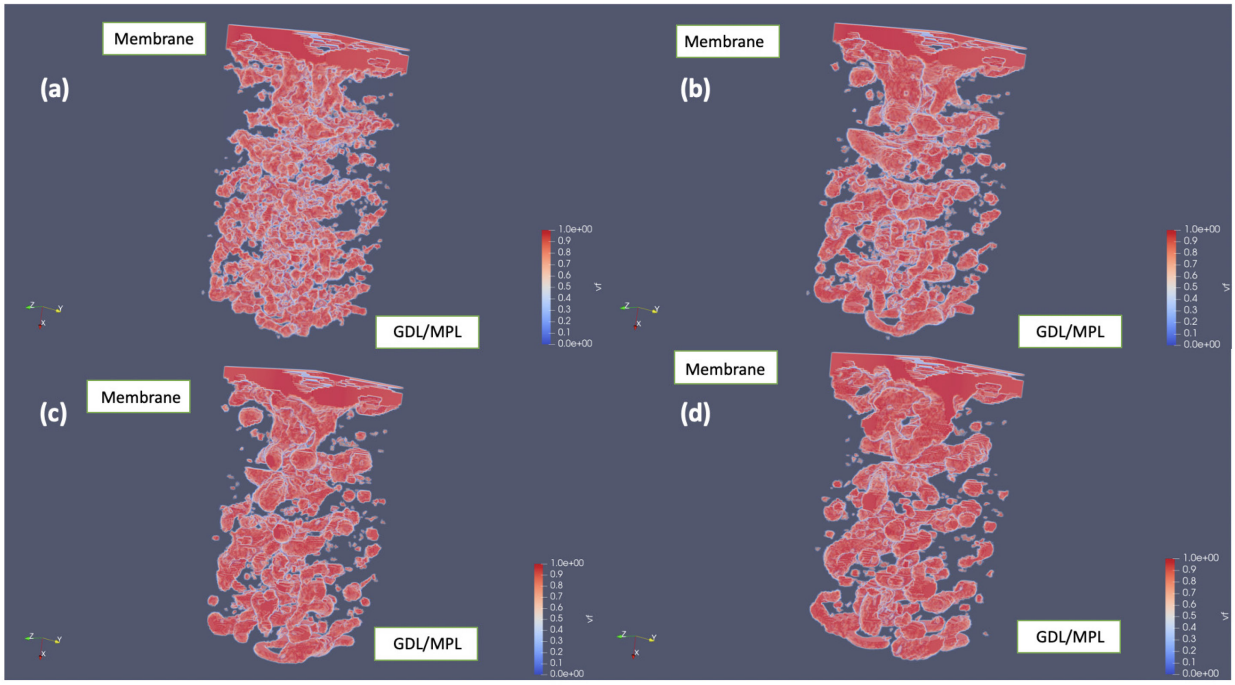


**Figure 9:** 90x90x181 RVE for the BOL electrode at various stages in the simulation towards steady-state at 3 MPa for filling portion of the simulation. (a) The geometry from the previous stage at time step 10000 (6 $\mu$s). (b) describes the geometry at time step 20000 (12 $\mu$s) at an intermediate point in the simulation. (c) describes the simulation at time step 35000 (21 $\mu$s). Finally, (d) is at time step 50000 (30 $\mu$s) where the simulation hit the convergence point.

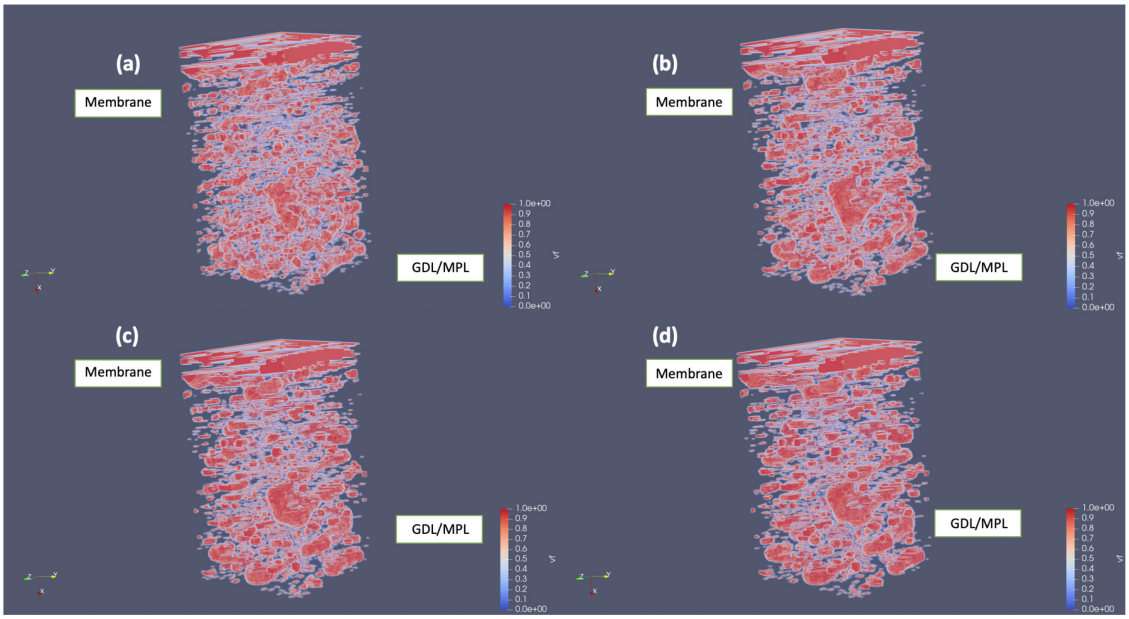


**Figure 10:** 90x90x154 RVE for the EOL electrode at various stages in the simulation towards steady-state at 3 MPa for filling portion of the simulation. (a) The geometry from the previous stage at time step 10000 (6 $\mu$s). (b) describes the geometry at time step 20000 (12 $\mu$s) at an intermediate point in the simulation. (c) describes the simulation at time step 35000 (21 $\mu$s). Finally, (d) is at time step 50000 (30 $\mu$s) where the simulation hit the convergence point.

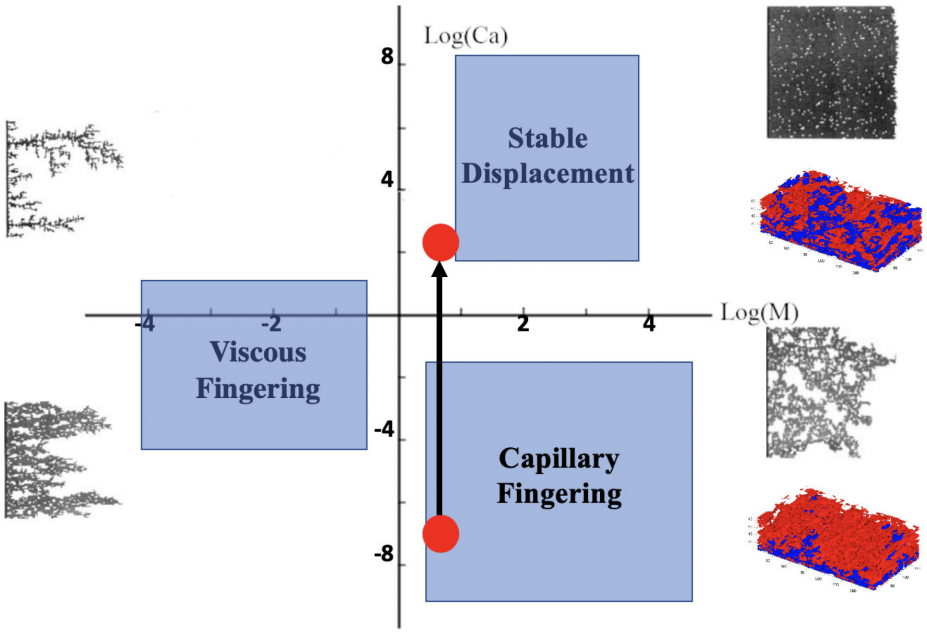


**Figure 11:** The phase diagram for the simulations in the CCL. Based on the dimensionless numbers (Ca and M, respectively), we see that we are in the region of capillary fingering in the beginning of simulation results (19.6 % saturation), which is what we see in the bottom right[104]. This gradually rises to what we see at the end of the simulation (85 % saturation), represented in the top right. The circle and arrow represent where the capillary number and viscosity ratio begin and end from low to high capillary pressures.

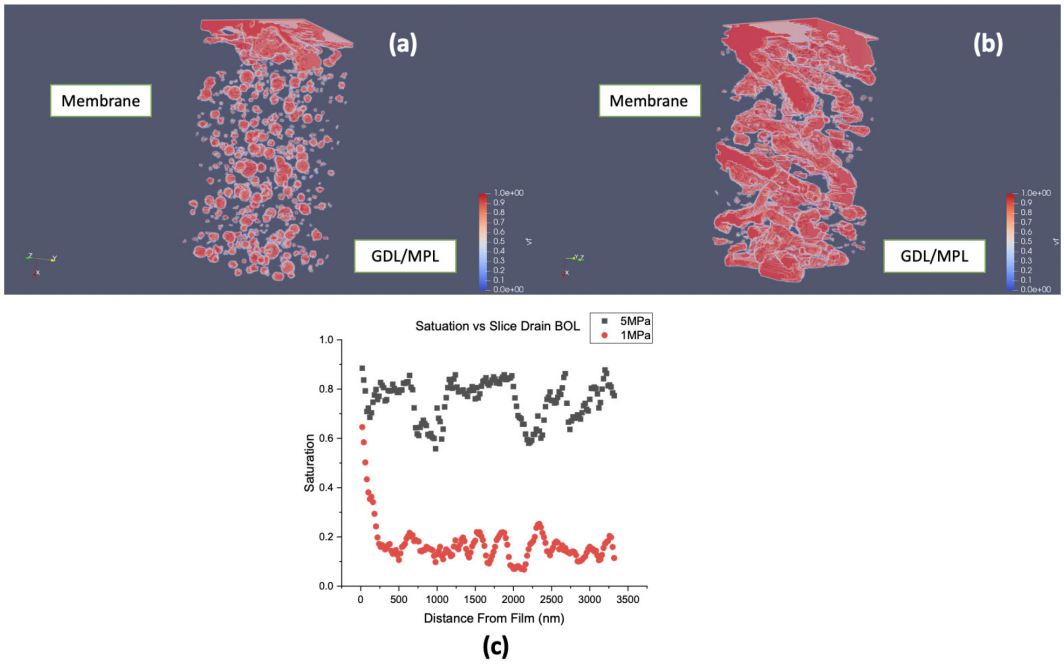


**Figure 12:** Drain portions of the curve for 5 MPa (a) and 1 MPa (b), as well as their slice comparison for different saturation levels (c) for the BOL Electrode.

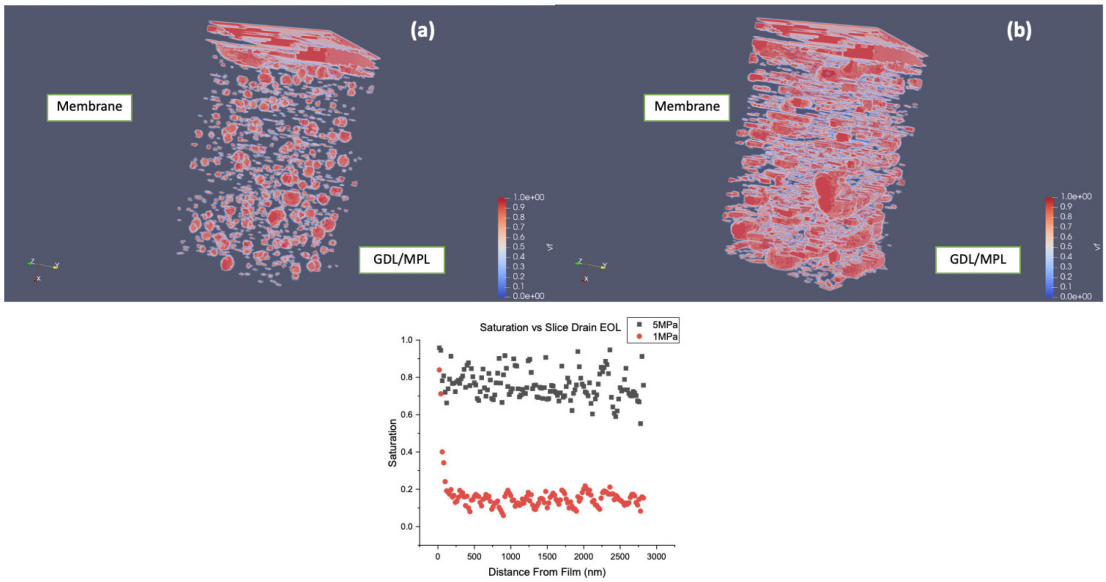


**Figure 13:** Drain portions of the curve for 5 MPa (a) and 1 MPa (b), as well as their slice comparison for different saturation levels (c) for the EOL electrode.

**Table 1:**

| Geometry | Size | Physical Units ($\mu$m) | Corrosion % |
|---|---|---|---|
| **BOL** | 90x90x181 | 0.225 x 0.225 x 3.62 | 0% |
| **Intermediate** | 90x90x90 | 0.451 x 0.587 x 1.80 | 34% |
| **EOL** | 90x90x154 | 0.225 x 0.286 x 3.08 | 43.4% |